Front. Earth Sci. 2019, 13(4): 817–828
https://doi.org/10.1007/s11707-019-0783-7

RESEARCH ARTICLE

The evolution of hollow symmetric-PV tower during the landfall of Typhoon Mujigae (2015)

Baofeng JIAO[1,2,3,4], Lingkun RAN[4,5], Xinyong SHEN (✉)[1,2,3,6]

1 Key Laboratory of Meteorological Disaster, Ministry of Education, Nanjing University of Information Science and Technology, Nanjing 210044, China
2 Joint International Research Laboratory of Climate and Environment Change, Nanjing University of Information Science and Technology, Nanjing 210044, China
3 Collaborative Innovation Center on Forecast and Evaluation of Meteorological Disasters, Nanjing University of Information Science and Technology, Nanjing 210044, China
4 Institute of Atmospheric Physics, Chinese Academy of Sciences, Beijing 100029, China
5 University of Chinese Academy of Sciences, Beijing 100029, China
6 Southern Marine Science and Engineering Guangdong Laboratory (Zhuhai), Zhuhai 519082, China

Abstract The evolution of Typhoon Mujigae (2015) during the landfall period is determined using potential vorticity (PV) based on a high-resolution numerical simulation. Diabatic heating from deep moist convections in the eyewall produces a hollow PV tower extending from the lower troposphere to the middle levels. Since the potential temperature and wind fields could be highly asymmetric during landfall, the fields are divided into symmetric and asymmetric components. Thus, PV is split into three parts: symmetric PV, first-order asymmetric PV, and quadratic-order asymmetric PV. By calculating the azimuth mean, the first-order term disappears. The symmetric PV is at least one order of magnitude larger than the azimuthal mean quadratic-order term, nearly accounting for the mean cyclone. Furthermore, the symmetric PV tendency equation is derived in cylindrical coordinates. The budget terms include the symmetric heating term, flux divergence of symmetric PV advection due to symmetric flow, flux divergence of partial first-order PV advection due to asymmetric flow, and the conversion term between the symmetric PV and quadratic-order asymmetric term. The diagnostic results indicate that the symmetric heating term is responsible for the hollow PV tower generation and maintenance. The symmetric flux divergence largely offsets the symmetric heating contribution, resulting in a horizontal narrow ring and vertical extension structure. The conversion term contribution is comparable to the mean term contributions, while the contribution of the partial first-order PV asymmetric flux divergence is apparently smaller. The conversion term implicitly contains the combined effects of processes that result in asymmetric structures. This term tends to counteract the contribution of symmetric terms before landfall and favor horizontal PV mixing after landfall.

Keywords landfall typhoon, potential vorticity, hollow PV tower, asymmetric features

Received March 31, 2019; accepted July 31, 2019

E-mail: shenxy@nuist.edu.cn

1 Introduction

Destructive winds and tremendous rainfall accompanied by landfall tropical cyclones (TCs) always result in severe disasters and serious losses (Duan et al., 2014). The distribution of disasters is closely related to the variabilities in intensity and structure of typhoons, which are still challenging for both researchers and forecasters (Montgomery and Smith, 2014). During the past few decades, limited improvements have been achieved in intensity changes compared with reducing track errors (Zhang et al., 2015). Wang and Wu (2004) mainly attributed the inapparent advance of intensity forecasting to the deficient understanding of internal and external processes as well as complex interactions.

Although the detailed mechanisms are complex and remain unclear, it is generally accepted that the evolution of the inner core is essentially responsible for intensity changes (Shapiro and Willoughby, 1982; Montgomery and Kallenbach, 1997; Schubert et al., 1999; Kossin and Eastin, 2001). The dynamics of the inner-core evolution have been extensively examined in terms of the eyewall evolution with a potential vorticity (PV) framework. The

cyclonic inflow at low levels spirals upward near the eyewall with a remarkable increase in PV, leading to a hollow PV structure in the mature TC. In the unforced idealized numerical model (Schubert et al., 1999; Kossin and Eastin 2001), the hollow PV tower satisfies the necessary barotropic instability condition, which tends to activate the eyewall breakdown and PV mixing between the eyewall and eye. This is one of the well-known dynamical mechanisms related to significant variability in intensity and structure. Considering the effects of diabatic heating and friction, Rozoff et al. (2009) found that barotropic instability is a transient brake during symmetric intensification. Except for reconfirming the basic conclusion, extensional studies by Hendricks et al. (2014) and Williams (2017) revealed that diabatic heating is responsible for producing the strengthening and thinning PV ring, while friction tends to stabilize the PV ring. Wu et al. (2009) examined a more realistic study with a full physics model. He noted that condensational heating is the key to maintaining the PV ring structure. Surface friction helps to maintain the PV ring when heating is present, whereas the PV mixing is enhanced when the heating fades. In addition, observational studies were also carried out with a main focus on eyewall mesovortices and horizontal mixing (Reasor et al., 2000; Kossin and Eastin, 2001).

In addition to investigations on quasi-axisymmetric vortexes, considerable asymmetric features, especially in the inner core, have gained research attention in recent decades. Increasing evidence indicates that internal asymmetric features play an important role in intensity and structure variability (Wang and Holland, 1996; Kuo et al., 1999; Reasor et al., 2000; Wang Y, 2002; Chen and Yau, 2003; Corbosiero et al., 2005). The asymmetric dynamics of TCs have been explored in a series of theories, including vortex Rossby waves (VRWs), barotropic instability and eyewall mixing, vertical hot towers, and vacillation cycles between symmetric and asymmetric structures (Montgomery and Kallenbach, 1997; Schubert et al., 1999; Montgomery et al., 2006; Nguyen et al., 2011). Montgomery and Smith (2014) emphasized the intrinsically non-axisymmetric nature of TCs. The asymmetric convections acting as stochastic or probabilistic perturbations significantly contribute to the large-scale circulation. The complex eddy-mean flow interaction makes the intensification problem more difficult and challenging.

Previous studies have revealed many of the fundamental characteristics of the internal dynamic evolution with a PV framework. Since the distribution of diabatic heating, potential temperature and wind flow exhibit remarkable asymmetric features during development or landfall periods, the relative importance of symmetric and asymmetric processes in relation to evolution requires further investigation. The purpose of this paper is to separate the contributions of symmetric processes from those of asymmetric processes during the landfall period of Typhoon Mujigae (2015). Considering the difficulty in obtaining high-resolution observations, a simulation of a real case is conducted with the WRF model (advanced research core of the Weather Research and Forecasting model). The tendency equation of the symmetric PV is derived in cylindrical coordinates and examined based on the simulation. This paper is organized as follows. In Section 2, the configuration of the numerical model as well as the intensity and structure evolution at different stages during the landfall period are presented. In Section 3, the detailed derivation of the azimuthal mean budget equation is given, and the key processes responsible for the evolution of the symmetric PV tower are determined. Concluding remarks and a summary are given in Section 4.

2 The evolution of Typhoon Mujigae (2015)

2.1 Numerical simulation

Typhoon Mujigae (2015) made landfall on Zhanjiang city, Guangdong Province, with robust strength after a rapid development period over the South China Sea, and broke the record since 1949 (Su et al., 2016). Strong winds and heavy rainfall as well as tornados in Foshan city resulted in severe casualties and economic losses. Jiao et al. (2017) performed a high-resolution numerical simulation of Mujigae with the WRF model. Verifications against observations indicate that the simulation can reasonably capture the dominant characteristics of Mujigae, including the general track, minimum sea level pressure, maximum surface wind preceding landfall as well as the kinematics, thermodynamic, and precipitation structures. The coarse domain of Jiao et al. (2017) is extended here using a grid size of 2 km. This simulation covers 30 h beginning at 1200 UTC 03 Oct, and during this time, Typhoon Mujigae reached its peak and made landfall over the western coast of Guangdong. WSM 6-class microphysics, CAM longwave radiation and shortwave radiation scheme, Pleim-Xiu land surface scheme, and ACM2 boundary-layer scheme are adopted. The initial condition is provided by the Goble Forecast System (GFS), while the boundary condition is interpolated from the coarse domain.

2.2 Temporal variation of intensity

Figure 1(a) compares the simulated intensity with the best track data issued by the Japan Meteorological Agency (JMA) and China Meteorological Administration (CMA) in terms of minimum sea level pressure and maximum surface wind speed. The simulation reasonably reproduces significant deepening before 0000 UTC 4, a relatively steady or mature state followed, and sharp weakening occurred after 0600 UTC 4, which is nearly identical to the two data sets despite some differences in details. The simulation is sampled every 10 min, and the observations are sampled every 6 h, and thus, the simulation exhibits

more fluctuations in intensity changes, especially in terms of the maximum surface wind speed. During the intensification period, the average deepening rate is nearly 2.5 hPa/h (and 1.25 m/(s·h)) from 1200 UTC 3 to 0000 UTC 4. This indicates that a prominent deepening precedes the landfall. From 0000 UTC 4 to 0600 UTC 4, the storm reaches its peak intensity and eventually makes landfall with the intensity situated between the observations. The storm transforms to the weakening stage after landfall with a mean rate of −3.3 hPa/h (and −2.3 m/(s·h)) from 0600 UTC 4 to 1800 UTC 4, decaying slightly faster than the observations.

To discuss the general evolution of PV in the inner core region, Fig. 1(b) shows the time series of the area-averaged PV and diabatic heating rate in a subdomain of 80 km × 80 km centered on the eye considering the inner core size of the storm, superposed with the potential temperature at the center. Notably, the evolution of the area-averaged PV is quite consistent with the intensity changes, increasing over the sea and decreasing over the land. The three-dimensional Rossby-Ertel PV equation with diabatic frictionless effects (Schubert et al., 1999) is as follows:

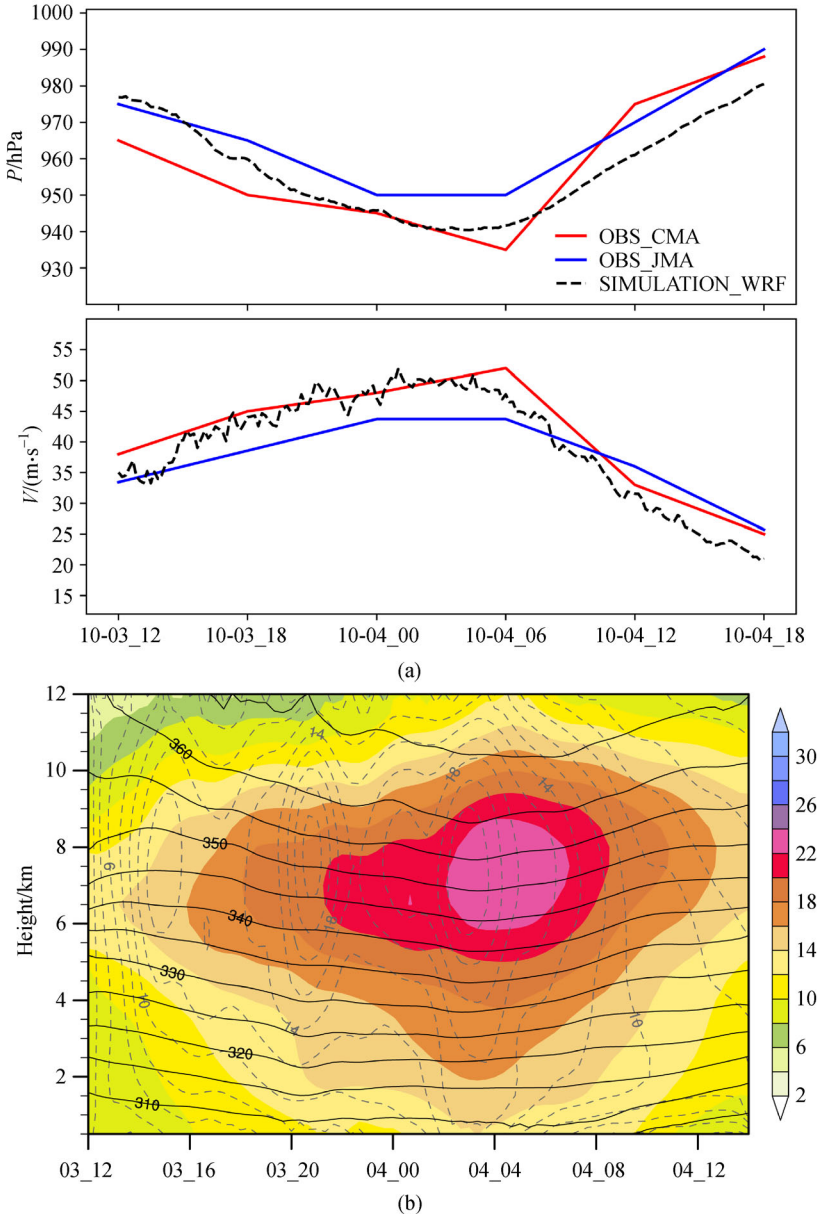

Fig. 1 Time series of (a) the minimum sea level pressures (hPa) (top panel) and the maximum symmetric surface wind speed (m/s) (bottom panel) for the WRF simulation (black dashed line) and observations issued by CMA (red solid line) and JMA (blue solid line); and the (b) time-height cross section of area-averaged PV (shaded, PVU) and diabatic heating rate (gray dashed line, interval = 2 K/h) in a subdomain of 80 km × 80 km centered around the eye, superposed with potential temperature (black solid line, interval = 5 K) at the center.

$$\frac{D}{Dt}(\alpha\boldsymbol{\eta}\cdot\nabla\theta)=\alpha\boldsymbol{\eta}\cdot\nabla\dot{\theta}, \quad (1)$$

where D/Dt is the material derivative, α is the specific volume, $\boldsymbol{\eta}=\nabla\times\boldsymbol{V}+f$ is the absolute vorticity vector, θ is the dry potential temperature, and $\dot{\theta}$ is diabatic heating. This indicates that the material increase in PV is mainly due to the heating term ($\alpha\boldsymbol{\eta}\cdot\nabla\dot{\theta}$). Figure 1(b) shows that a large cyclonic PV is mainly concentrated in the mid-troposphere and extends from 4 km to 9 km. During the intensification stage before landfall, three diabatic heating centers are found near the height of 7 km. The most remarkable center occurs ahead of the intensity peak, and noteworthy diabatic heating extends from the surface to approximately 10 km. The area-averaged PV increases rapidly at all levels and is especially prominent at the corresponding moment associated with extensive heating. After landfall, the diabatic heating rate as well as the gradient decrease sharply. The area-averaged PV begins to decrease, which is consistent with the sea level pressure and maximum surface wind speed tendencies shown in Fig. 1(a).

The results confirm that the simulation reasonably reproduces Typhoon Mujigae with remarkable deepening before landfall and sharp weakening after landfall. The evolution of the area-averaged PV is consistent with the intensity trend.

2.3 Structure and evolution characteristics of PV

To further understand the evolution of PV, detailed vertical and horizontal structures must be explored at different stages. Figure 2 shows the cross section of the azimuthal averaged PV and transverse circulation superposed with the axisymmetric diabatic heating rate at selected times, and Fig. 3 depicts the corresponding detailed horizontal distribution of PV and the associated wind field at a height of 1.5 km. Notably, symmetric or asymmetric analyses are very sensitive to the vortex center detection accuracy. In

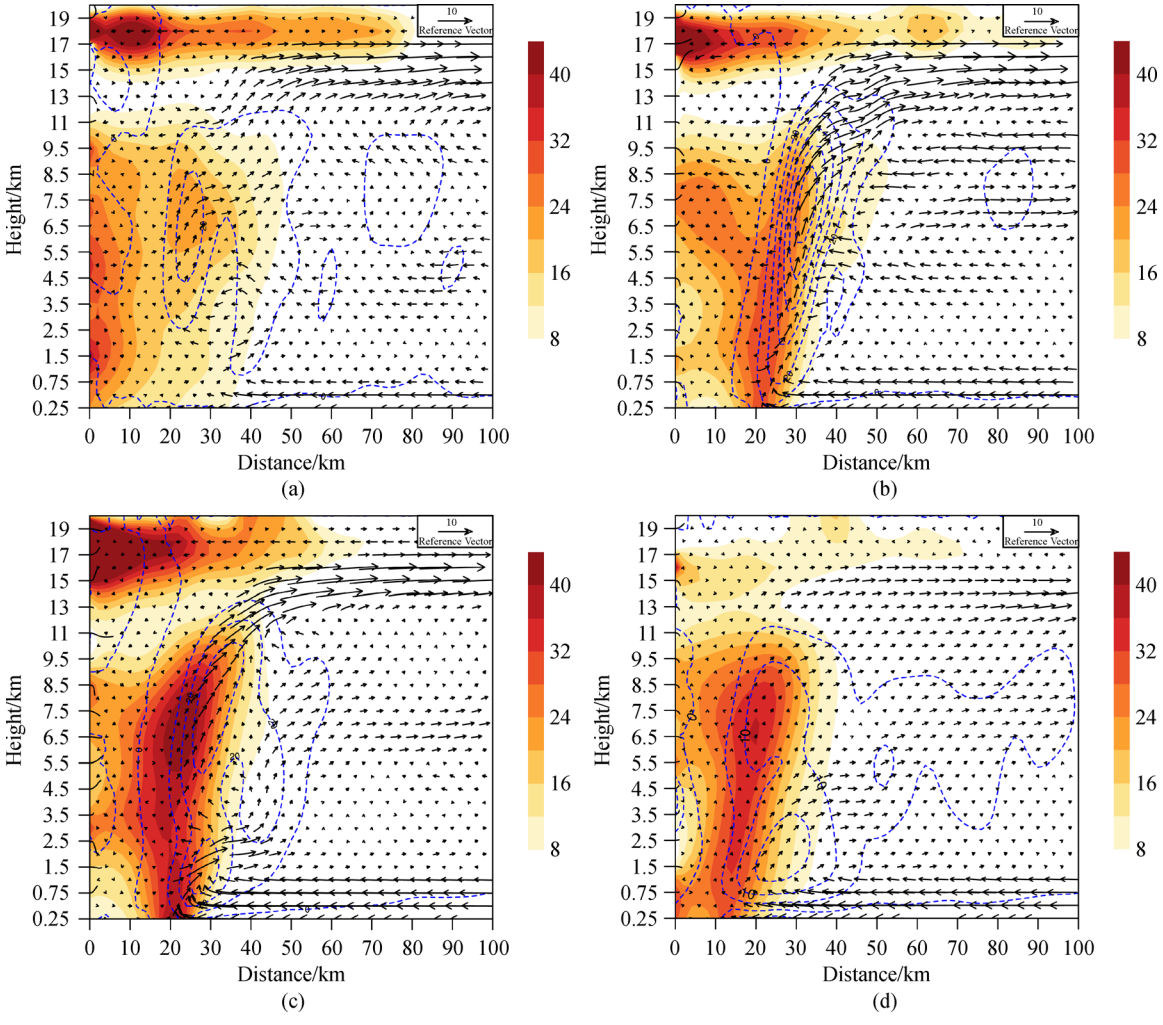

Fig. 2 Vertical cross section of axisymmetric PV (shaded, PVU), diabatic heating rate (blue dashed line, interval = 10 K/h in a, b, and c, and the interval = 5 K/h in d), and wind vectors (m/s) at (a) 1700 UTC 3, (b) 2000 UTC 3, (c) 0400 UTC 4, and (d) 1000 UTC 4.

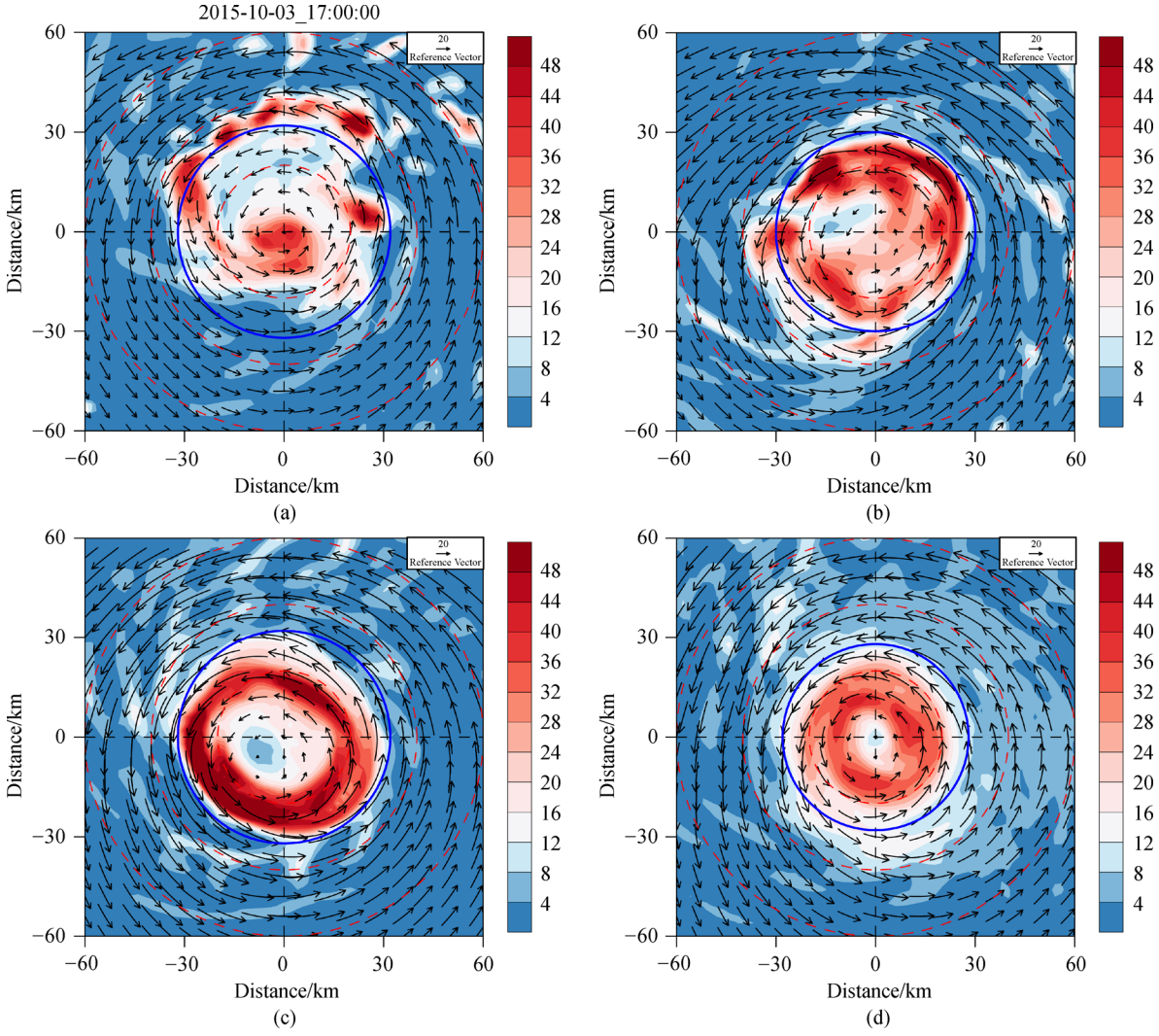

Fig. 3 Horizontal PV (shaded, PVU) and wind vector (m/s) at the 1.5 km height at (a) 1700 UTC 3, (b) 2000 UTC 3, (c) 0400 UTC 4, and (d) 1000 UTC 4. X-coordinates and y-coordinates represent the distance to the vortex center (km). The red dashed circles are placed at radii of 20, 40, and 60 km from the center. The blue solid circle indicates the maximum wind radius.

this paper, the center is first estimated by the minimal point of sea level pressure, which is followed by an adjustment based on the idea that the maximal azimuth averaged tangential wind at the height of 1.5 km should be the highest if the point is close to the vortex center (Kurihara et al., 1993, 1995). Once the center is detected in the model, all the components as well as the maximum wind radius are achieved.

During the intensification period at 1700 UTC 3 (Fig. 2(a)), a high PV occupies the core, which is called a monopole PV structure. Excluding the possibility of newly formed mesoscale convection in the core, this structure may be attributed to either inaccuracy detection of the vortex center or inner core vacillation cycles (Nguyen et al., 2011). The secondary circulation is weak, with the maximum vertical winds occurring at mid-levels. Diabatic heating released in the weak updraft is responsible for the additional high PV at the height of 6.5 between the radii of 20 km and 30 km. After several hours (at 2000 UTC 3, Fig. 2(b)), the PV in the eye deceases to less than 16 PVU in the low and mid-troposphere, while that situated just inside the eyewall is amplified both in range and values. The monopole PV structure is destroyed and converted to a hollow structure. There is strong updraft throughout the troposphere tilting outward in the eyewall. Diabatic heating increases remarkably within the strong updraft, indicating the much well-organized convections are concentrated in the eyewall. When the typhoon approaches its peak intensity prior to landfall (at 0400 UTC 4, Fig. 2(c)), the distribution of the PV still shows a hollow structure with a high PV inside the eyewall and low PV in the eye. However, inflow in the boundary layer is dramatically enhanced. The enhanced inflow turns over near the radius of the maximum wind, flowing outward radially at the top of the boundary, which is responsible for the secondary heating center near the top of the boundary layer. During the weakening period after

landfall (Fig. 2(d)), diabatic heating and updraft decrease sharply with the loss of sea surface energy supply and cannot maintain the hollow structure. The PV ring gradually transforms to a monopolar structure from low levels, indicating a bridge-like structure near 1.5 km.

The asymmetric features of the PV and horizontal winds are noteworthy in Fig. 3. At 1700 UTC 3 (Fig. 3(a)), particles with PVs exceeding 36 PVU settle into the vortex center, while several separated patches with high PV circles are found around the eye between radii of 20 km and 40 km. This represents the evolving and chaotic distribution of intense convections. A broad region with a PV of less than 12 PVU is located north-west of the center. As the vortex continues to deepen (Fig. 3(b)), separated patches contract inward, coalescing into an incompletely organized annular PV band inside the maximum wind radius. The region with a low PV shrinks significantly and is surrounded by the band. Particles in the center move outward and merge with the incompletely organized PV band. The horizontal structure is expected to be a hollow PV tower with low values in the vortex center and high values near the eyewall. When the storm reaches its peak intensity (Fig. 3(c)), the PV ring is completely closed and becomes more symmetric despite the elliptic eye. The region with a low PV is more concentrated around the center. The reversal of the radial gradient PV satisfies the condition of combined barotropic-baroclinic instability. However, it holds the structure until the sharp weakening occurs over the land. After landfall (Fig. 3(d)), the PV ring contracts inward, and the intensity remarkably decreases with three separated centers. A large PV in the eyewall is mixed into the eye. The hollow ring gradually converts to a monopole structure.

The PV features during the landfall period are presented with both vertical and horizontal structures. Considerable asymmetric characteristics of the PV and wind fields are associated with the buildup and breakdown of the hollow tower structure. The relative importance of the asymmetric terms is still unclear. The contribution of symmetric and asymmetric processes will be discussed in the next section with the analysis of the symmetric PV tendency.

3 Budget diagnostics

In this section, all fields are partitioned into symmetric and asymmetric components. Thus, PV is split into three parts: symmetric PV, first-order asymmetric PV, and quadratic-order asymmetric PV. The tendency equations of the symmetric PV and azimuthal mean quadratic-order term are derived in cylindrical coordinates. In the remainder, budget diagnostics of symmetric PV are performed to investigate the major kinematic and thermodynamic process involved with a focus on the roles of symmetric asymmetric processes.

3.1 Budget equation

A three-dimensional, compressible, inviscid, diabatic, nonhydrostatic flow on the f plane is considered. The momentum and thermodynamic equations in cylindrical coordinates are as follows:

$$\frac{\partial \boldsymbol{V}}{\partial t}+\boldsymbol{V}\cdot\nabla\boldsymbol{V}+\left(f_0+\frac{v}{r}\right)\boldsymbol{k}\times\boldsymbol{V}=-\frac{1}{\rho}\nabla p-g\boldsymbol{k}, \quad (2)$$

$$\frac{\partial \theta}{\partial t}+\boldsymbol{V}\cdot\nabla\theta=S, \quad (3)$$

where $\nabla=\boldsymbol{r}\frac{\partial}{\partial r}+\boldsymbol{\lambda}\frac{\partial}{r\partial\theta}+\boldsymbol{k}\frac{\partial}{\partial z}$, r, $\boldsymbol{\lambda}$, and k represent the unit vectors in the radial, azimuthal and vertical directions; $\boldsymbol{V}=(u,v,w)$ is the three-dimensional vorticity, namely, the radial, tangential, and vertical winds, respectively; f_0 is the Coriolis parameter; ρ is the density; p is the pressure, g is the gravitational acceleration; θ is the dry potential temperature; and S is the diabatic heating rate (in Kelvins per second). We define the flux form equation as follows:

$$q=\boldsymbol{\eta}\cdot\nabla\theta. \quad (4)$$

Taking the temporal partial derivative of (4), one can obtain the budget equation after eliminating the tendency terms with Eqs. (2) and (3):

$$\frac{\partial q}{\partial t}+\nabla\cdot(\boldsymbol{V}\cdot q)=\nabla\cdot(\boldsymbol{\eta}\cdot S). \quad (5)$$

The equation indicates the conserved PV is related to transport, including internal heating and advective flux. Let $X=X_{\mathrm{s}}+X_{\mathrm{a}}$ with X being u,v,w,p,ρ,θ,S, where X_{s} denotes the symmetric component and X_{a} denotes the asymmetric part. Thus, q can be decomposed into three portions:

$$q=q_{\mathrm{s}}+q_{\mathrm{e}}+A, \quad (6)$$

where

$$q_{\mathrm{s}}=\boldsymbol{\eta}_{\mathrm{s}}\cdot\nabla\theta_{\mathrm{s}}, \quad (7)$$

$$q_{\mathrm{e}}=\boldsymbol{\eta}_{\mathrm{s}}\cdot\nabla\theta_{\mathrm{a}}+\boldsymbol{\eta}_{\mathrm{a}}\cdot\nabla\theta_{\mathrm{s}}, \quad (8)$$

$$A=\boldsymbol{\eta}_{\mathrm{a}}\cdot\nabla\theta_{\mathrm{a}}, \quad (9)$$

are the symmetric, first-order asymmetric and quadratic-order asymmetric PVs, respectively. q_{s} is the projection of symmetric vorticity onto the gradient of symmetric potential temperature, presenting the dynamical property of symmetric systems; q_{e} is the first-order in disturbance amplitude describing the bulk properties of both symmetric and asymmetric systems; A is the quadratic in the asymmetric fields, and in nature, this is a type of eddy energy. A can depict the dynamical characteristics of locally asymmetric systems. These portions are not independent, which can be illustrated by the budget equations. Substituting the partitioned variables into Eq. (5), the equation is expanded as follows:

$$\frac{\partial}{\partial t}(q_s + q_e + A) + \nabla\cdot[(\boldsymbol{V}_s + \boldsymbol{V}_a)\cdot(q_s + q_e + A)]$$

$$-\nabla\cdot[(\boldsymbol{\eta}_s + \boldsymbol{\eta}_a)\cdot(S_s + S_a)] = 0. \quad (10)$$

The budget equation for the mean cyclone similar to that in Wang (2002) can be achieved by performing an azimuth mean on the left side of (10):

$$\frac{\partial}{\partial t}(q_s + \langle A\rangle) + \nabla\cdot(\boldsymbol{V}_s q_s + \langle \boldsymbol{V}_a q_e\rangle + \boldsymbol{V}_s\langle A\rangle + \langle \boldsymbol{V}_a A\rangle)$$

$$-\nabla\cdot(\boldsymbol{\eta}_s S_s + \langle \boldsymbol{\eta}_a S_a\rangle) = 0, \quad (11)$$

where $\langle\ \rangle$ represents the azimuthally averaged operator. The symmetric PV is one or two orders of magnitude larger than the quadratic-order term. Thus, the evolution is nearly responsible for the evolution of the mean vortex, which motivates separation of the q_s tendency to identify the dominant processes and investigate the potential relationship between q_s and $\langle A\rangle$. The budget of the symmetric PV can be written as follows (see Appendix):

$$\frac{\partial q_s}{\partial t} = \nabla\cdot(\boldsymbol{\eta}_s S_s) - \nabla\cdot(\boldsymbol{V}_s q_s) - \nabla\cdot\langle \boldsymbol{V}_a q_{e1}\rangle$$

$$+ \nabla\cdot\langle F_{ex}\rangle, \quad (12)$$

where $q_{e1} = \boldsymbol{\eta}_s\cdot\nabla\theta_a$, $\langle F_{ex}\rangle = -\langle\nabla\theta_a\times(\boldsymbol{\eta}_s\times\boldsymbol{V}_a)\rangle + \nabla\theta_s \times\langle -\frac{\rho_a}{\rho_s^2}\nabla p_a\rangle$.

The budget of the azimuthal-mean quadratic-order PV is given as follows:

$$\frac{\partial\langle A\rangle}{\partial t} = \nabla\cdot\langle\boldsymbol{\eta}_a S_a\rangle - \nabla\cdot\langle\boldsymbol{V}_s A\rangle - \nabla\cdot\langle\boldsymbol{V}_a q_{e2}\rangle$$

$$-\nabla\cdot\langle\boldsymbol{V}_a A\rangle - \nabla\cdot\langle F_{ex}\rangle, \quad (13)$$

where $q_{e2} = \boldsymbol{\eta}_a\cdot\nabla\theta_s$. Equation (12) describes the evolution of the symmetric PV. The first two terms on the right-hand side denote the flux divergence related to symmetric diabatic heating (DIAS) and the symmetric flow (FDM), respectively. The third term is associated with the flux of the partial first-order PV due to asymmetric motion (FDE). The fourth term means the conversion rate between q_s and $\langle A\rangle$, representing the complex effects of the asymmetric features (FEX). The amplitude of the azimuthal perturbation pressure gradient force per unit mass is quadric orders smaller than the leading term and can be omitted in $\boldsymbol{F}_{ex}$. The local temporal change of $\langle A\rangle$ in Eq. (13) is dependent on asymmetric diabatic heating, the flux divergence including the quadratic-order PV flux caused by the symmetric flow, the rest of the first-order PV flux due to asymmetric motion, the flux due solely to the nonlinear eddy process, and the conversion rate corresponding to that in Eq. (12) with opposite signs. The azimuthal mean quadratic-order PV acts as the difference between the symmetric PV in previous work and that in this paper. Although it is not analyzed in this paper, the related features and budget would be an interesting investigation. Regardless, this should be a topic of future work.

3.2 Azimuthal mean budget diagnostics

A preliminary diagnostic analysis on the contributions of symmetric terms and asymmetric terms is performed based on the symmetric PV budget at the times corresponding to pre-landfall and post-landfall conditions. It is expected that both the symmetric and asymmetric terms will play a significant role in the evolution given the considerable asymmetric feature in the previous section. Since the terms in Eq. (12) describe the tendency of $q_s(q_s = \boldsymbol{\eta}_s\cdot\nabla\theta_s)$, the terms on both sides are divided by the averaged density (varies only with height) to make the results comparable among the different heights in the analysis.

Figure 4 depicts the budget terms valid at 0400 UTC 4. The storm remains over the sea and reaches its peak intensity at this moment. The hollow PV tower has some asymmetric characteristics (Fig. 3(c)). The local changes in the symmetric PV are mainly dominated by the symmetric diabatic heating term (DIAS), flux divergence of symmetric-PV due to symmetric flow (FDM), and the conversion term (FEX). Because the vorticity vector in the inner-core region generally points upward, the DIAS contribution is dependent on the vertical gradient of symmetric diabatic heating. Consistent with that in Williams (2017), the PV generation is found above the region of maximum heating, whereas the PV consumption is found below the region. The most striking difference between this real case simulation during landfall and idealized experiments is the occurrence of two maximum heating centers with the principal one at the height of 8 km and the secondary one at the top of the boundary (Fig. 2(c)), so do the generation and consumption center pairs (Fig. 4(a)). They represent the effects of condensational heating in the strong updraft and the frictional forced outflow layer just above the boundary inflow, respectively. The FDM contribution is generally the opposite, which indicates that the contribution of symmetric diabatic heating is largely offset by the symmetric PV advection due to symmetric secondary circulation. In other words, the FDM rearranges the heat forced PV production and helps to maintain the hollow structure with horizontal enhancement and vertical extension. Compared with the traditional diagnosis, the FDM contribution serves as little more than the symmetric advection effect of PV in the idealized experiments, reducing the PV at the outside edge of the heating region and adverting the high PV upward. In general, the symmetric terms tend to produce a thin PV ring inside the heating center.

In previous studies such as Wang (2002), the azimuthal

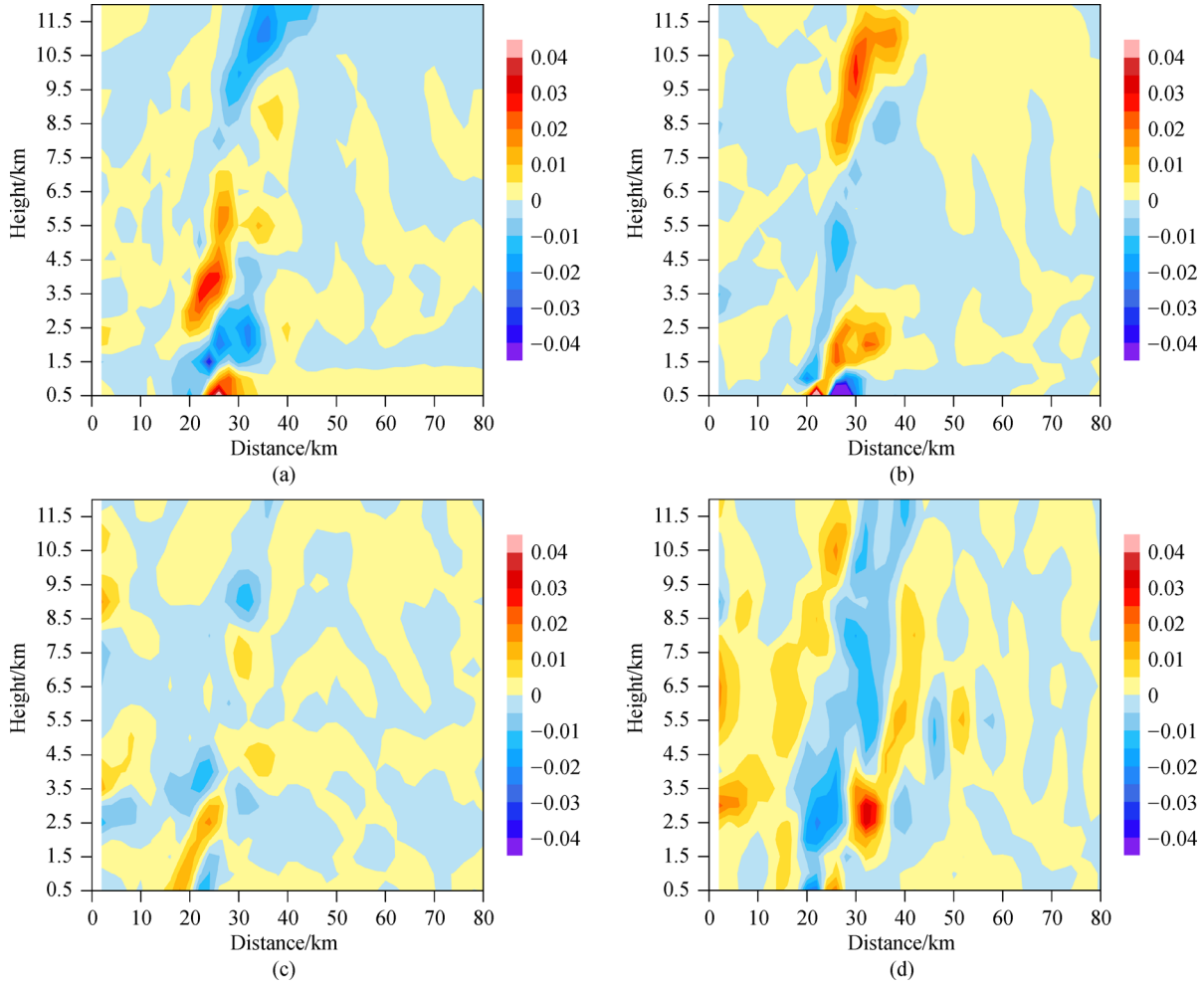

Fig. 4 Symmetric PV budget terms at 0400 UTC4: (a) DIAS, (b) FDM, (c) FDE, and (d) FEX (PVU/s). The x-coordinate indicates the distance to the center of the storm (km), while the y-coordinate represents height (km).

mean PV is equivalent to the summation of symmetric PV and azimuthal mean quadratic-order PV in this paper. As a result, the direct contributions of the symmetric PV caused by asymmetric structures have never been analyzed before. The asymmetric terms contain the contribution of the partial flux divergence of the first-order PV (Fig. 4(c)) and the exchange term (Fig. 4(d)) shared with the budget of $\langle A \rangle$. The contribution of FDE is small in value compared with the other terms with a positive production of less than 0.015 PVU/s within the PV ring at low levels. The value of FEX is obviously higher and comparable to the contribution of mean terms as expected (Fig. 4(d)). It features a negative contribution in the PV ring region and a positive contribution on either side. This tends to counteract the effects of the mean terms and lead to weakening of the PV ring. Although the specific processes are not explicitly included, the FEX term containing the asymmetric dry potential temperature and asymmetric wind vector reflects the total effect of the eddy-mean flow interaction and the asymmetric features caused by discontinuity of the surface characteristics or asymmetric diabatic heating. It is also notable that even the condition for the combined barotropic-baroclinic instability is satisfied since the formation of the PV ring, the ring does not breakdown during the intensification stage before landfall.

The storm begins to weaken after landfall. The PV ring tends to break down. Figure 5 depicts the budget terms valid at 1000 UTC 4. The symmetric secondary circulation decays rapidly due to the loss of diabatic heating and moist flux supply from the underlying ocean surface (Fig. 2(d)). The most striking feature in Fig. 5 is that the values of all the terms decrease to less than half of that in Fig. 4, with the maximum contracting inward to the center. The decrease in DIAS is directly related to the weak diabatic heating, while the FDM decreases due to the lower PV production and weaker secondary circulation. The generated PV is not enough to further maintain the PV ring structure, and it gradually breaks down from the low levels. The contribution of FDE is still the smallest compared with the other terms. The exchange term FEX shows a significant positive contribution inside the PV ring, especially at low levels, which is likely related to the

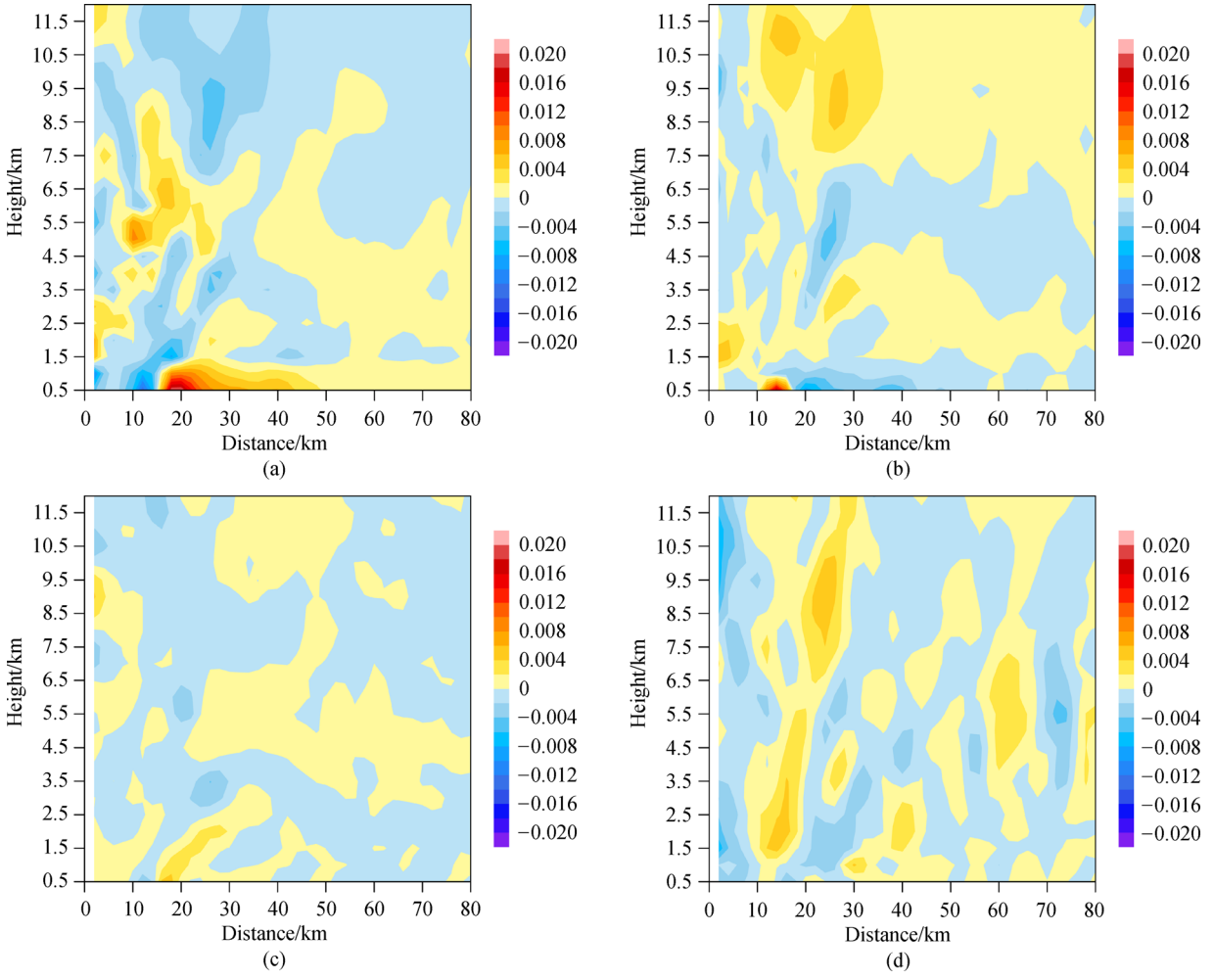

Fig. 5 Same as in Fig. 4 but at 1000 UTC 4.

development of asymmetric processes that mix high PV from the hollow PV tower to the eye region in an asymmetric manner.

3.3 The effect of landmass

As the Typhoon makes landfall, the landmass will result in significant changes in structure and intensity. The discontinuity between the land and sea surface tends to promote the development of asymmetric structures (Zhang et al., 1999; Wei et al., 2011). The loss of heat and moisture flux from the surface restricts the intensity of the storm (Chen and Yau, 2003). The increased surface friction plays dual roles, including serving as a dissipation term and enhancing boundary inflow as well as horizontal mixing (Wu et al., 2009). The complex topography in the track also plays a role in weakening the storm (Meng et al., 1998; Yu and Tan, 2007; Li et al., 2009). In the previous section, the roles of asymmetric features have been taken into consideration while the contribution of friction is excluded. When reconsidering the momentum Eq. (2) with the friction term, the direct impact of friction will appear on the right side of the budget Eq. (12), that is $\nabla\theta_s \cdot \nabla \times \boldsymbol{F}_s$, where $\boldsymbol{F}_s$ represents symmetric turbulent friction. Referring to Liu and Liu (2011), friction in the x direction in cartesian coordinates can be approximately expressed as $F_x = \alpha\frac{\partial}{\partial z}\left(\rho K\frac{\partial u}{\partial z}\right)$, where K is the momentum turbulent exchange coefficient in the vertical direction. The magnitude of the friction term in the budget equation may be estimated as 10^{-6} PVU/s, which is much smaller than the contributions of other terms. Thus, the friction term can be omitted from the right-hand side of the equation and has little impact on the accuracy.

Although the direct impact is negligible, friction can still affect the dynamic and thermodynamic structures of typhoons, which are extremely important to the storm evolution. The cross-section structures of Mujigae during landfall are described in Figure 6. Compared with the best track dataset (not shown), the simulated track is more

northward within an acceptable range as seen in Figure 4 of Jiao et al. (2017). On the cross section aligning with the translating direction at 0400 UTC 4 (Figure 6(a), from (110.44E, 21.41N) to (111.42E, 20.78N)), it is notable that the elevated PV columns at the front side are much larger than those in the rear quadrants. This is attributed to the extensive updraft. Surface friction is expected to be responsible for the low-level convergence and the enhanced inflow in the boundary. In addition, the enhanced inflow erodes the PV at the outer edge, narrowing the PV ring. After landfall at 1200 UTC 4 (Figure 6(b), from (109.74E, 22.3N) to (109.87E, 21.47N)), the cutoff of heat flux and moist flux from the underlying surface sharply decreases the convection and PV generation. The enhanced friction tends to promote the mixing process, indicated by the formation of bridge structures in the cross section or the monopolar structure at the plane of the low levels. In addition, the terrain plays an additional role in weakening the storm as well as the PV anomalies that are induced by mountains.

4 Conclusions and discussion

In this study, we examined the evolution of Typhoon Mujigae (2015) during the landfall period with a PV framework using a high-resolution simulation. The asymmetric processes and symmetric processes are separated in the symmetric PV budget. Primary determinations are made on the contributions of different terms before and after landfall. The primary results are as follows:

- Compared with the time series of minimal sea level pressure and maximal surface wind, the evolution of the area averaged PV is consistent with the intensity changes. The symmetric vertical structures depict the build-up and maintenance of the hollow ring before landfall and breakdown after landfall, while the detailed horizontal structures reveal the considerable asymmetric features in the inner-core region associated with the evolution of the typhoon during different stages.
- Analyzing the mean terms shows symmetric diabatic heating in the eyewall convections accounts for generation and maintenance of the hollow PV tower. It is largely offset by the flux divergence related to symmetric advection. The divergence of symmetric PV advection due to symmetric secondary circulation erodes the PV generations at the outer edge and extends the hollow structure from lower to middle troposphere.
- Analyzing the asymmetric terms shows that the contribution of asymmetric terms is comparable with that of the mean terms. The FDE contribution is relatively small compared with the contribution of FEX. FEX tends to decrease the values in the PV ring and increase on either side before landfall. After landfall, the FEX shows a significant positive contribution inside the PV ring, which is likely related to the development of the eddy processes that mix the high PV from the hollow PV tower with the eye region in an asymmetric manner.

These results are from this particular case, which is limited or unique to some extent. These results may not be directly applicable in other cases since the situations may vary greatly among different typhoon cases. However, the theoretical budget equation proposed in this paper can be applied to obtain the corresponding results. General features and common results need additional examinations with an adequate number of cases, which should be the topic of a future investigation.

In terms of disaster prevention and reduction, the evolution of TC intensity and structure could be roughly achieved based on the analysis of different forcing terms in the budget equation. Further, the direct disasters, including strong winds and torrential rain, would be reasonably assessed as well as the secondary disasters. This assessment serves as the basis of disaster reduction and prevention in advance. Notably, the results in this particular case strongly suggest that more attention should

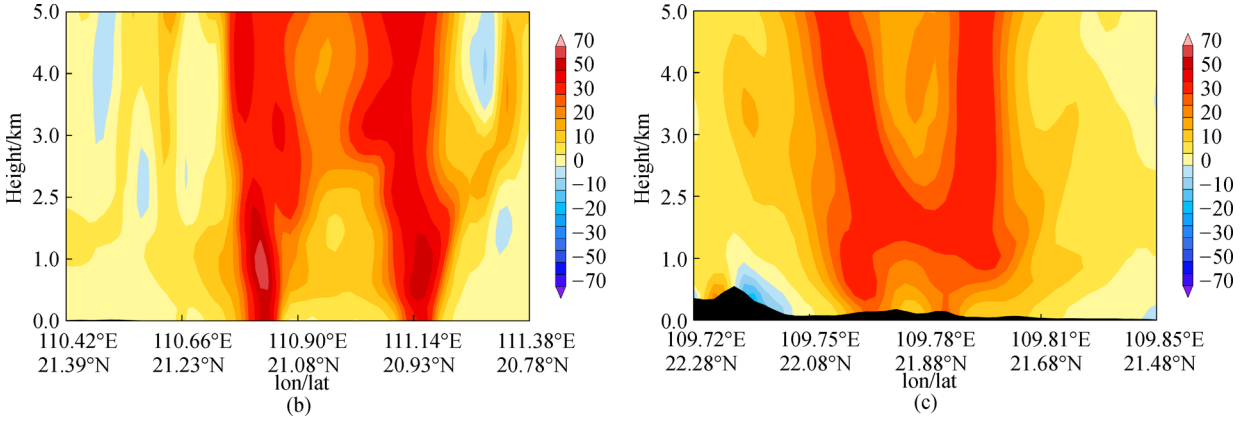

Fig. 6 The cross section of PV (shaded, PVU) (a) from (110.44E, 21.41N) to (111.42, 20.78N) at 0400 UTC 4, and (b) from (109.74E, 22.3N) to (109.87E, 21.47N) at 1200 UTC 4.

be given to the asymmetric structures. Asymmetric structures seem to significantly affect the evolution of the symmetric-PV with contributions that are comparable to the symmetric processes.

Acknowledgements This study was supported by the Strategic Leading Science and Technology Project (A) of the Chinese Academy of Sciences (Grants Nos. XDA17010105 and XDA20100304), the National Basic Research Program of China (Grants No. 2015CB452804), and the National Natural Sciences Foundation of China (Grant Nos. 41575065, 4177510, and 41530427), and The Key Projects of Jilin Province Science and Technology Development Plan (Grants No. 20180201035SF).

Appendix

We re-examine Eqs. (2) and (3) with variable partitioning. By performing an azimuthal average after the decomposition, the symmetric equations can be written as follows:

$$\nabla\times\left[\frac{\partial \boldsymbol{V}_s}{\partial t}+\boldsymbol{\eta}_s\times\boldsymbol{V}_s+\frac{1}{\rho_s}\nabla p_s+\langle\boldsymbol{\eta}_a\times\boldsymbol{V}_a-\frac{\rho_a}{\rho_s^2}\nabla p_a\rangle\right]=0, \tag{A1}$$

$$\frac{\partial\theta_s}{\partial t}+\boldsymbol{V}_s\cdot\nabla\theta_s+\langle\boldsymbol{V}_a\cdot\nabla\theta_a\rangle=S_s. \tag{A2}$$

Taking the temporal partial derivative of (7), one obtains the following equation:

$$\frac{\partial q_s}{\partial t}=\nabla\left(\boldsymbol{\eta}_s\frac{\partial\theta_s}{\partial t}-\nabla\theta_s\times\frac{\partial\boldsymbol{V}_s}{\partial t}\right). \tag{A3}$$

Substituting (A1) and (A2) into (A3), the tendency terms in the right hand side of (A3) can be eliminated. The tendency of the symmetric PV can be obtained in the following form:

$$\frac{\partial q_s}{\partial t}=\nabla\cdot(\boldsymbol{\eta}_s S_s)-\nabla\cdot(\boldsymbol{V}_s q_s)-\nabla\cdot\langle\boldsymbol{V}_a q_{e1}\rangle+\nabla\cdot\langle\boldsymbol{F}_{ex}\rangle \tag{A4}$$

where $q_{e1}=\boldsymbol{\eta}_s\cdot\nabla\theta_a$, $\langle\boldsymbol{F}_{ex}\rangle=-\langle\nabla\theta_a\times(\boldsymbol{\eta}_s\times\boldsymbol{V}_a)\rangle+\nabla\theta_s\times\langle\boldsymbol{\eta}_a\times\boldsymbol{V}_a\rangle+\nabla\theta_s\times\langle-\frac{\rho_a}{\rho_s^2}\nabla p_a\rangle$.

We can obtain the budget equation for the azimuthal mean quadratic-order PV from Eqs. (2) and (3) by taking the temporal partial derivative of (9) and following the same method mentioned above. Alternatively, the budget equation for $\langle A\rangle$ can also be directly obtained by subtracting Eq. (12) from Eq. (11).

References

Chen Y, Yau M K (2003). Asymmetric structures in a simulated landfalling hurricane. J Atmos Sci, 60(18): 2294–2312

Corbosiero K L, Molinari J, Black M L (2005). The structure and evolution of Hurricane Elena (1985). Part I: Symmetric intensification. Mon Weather Rev, 133(10): 2905–2921

Duan Y H, Chen L S, Liang J Y, Wang Y, Wu L G, Cui X P, Ma L M, Li Q Q (2014). Research progress in the unusual variations of typhoons before and after landfalling. Acta Meteorol Sin, 72(5): 969–986 (in Chinese)

Hendricks E A, Schubert W H, Chen Y H, Kuo H C, Peng M S (2014). Hurricane eyewall evolution in a forced shallow-water model. J Atmos Sci, 71(5): 1623–1643

Jiao Y Y, Ran L K, Li N, Gao S T, Zhou G B (2017). High resolution numerical simulation of Typhoon Mujigae (2015) and analysis of vortex Rossby waves. Wuli Xuebao, 66(08): 381–400 (in Chinese)

Kossin J P, Eastin M D (2001). Two distinct regimes in the kinematic and thermodynamic structure of the hurricane eye and eyewall. J Atmos Sci, 58(9): 1079–1090

Kuo H C, Williams R T, Chen J H (1999). A possible mechanism for the eye rotation of Typhoon Herb. J Atmos Sci, 56(11): 1659–1673

Kurihara Y, Bender M A, Ross R J (1993). An initialization scheme of hurricane models by vortex specification. Mon Weather Rev, 121(7): 2030–2045

Kurihara Y, Bender M A, Tuleya R E, Ross R J (1995). Improvements in the GFDL hurricane prediction system. Mon Weather Rev, 123(9): 2791–2801

Li Y, Qian C H, Chen L S (2009). A study on the eyewall expansion of Typhoon Sepat (2009) during its landfall process. Acta Meteorol Sin, 67(5): 799–810 (in Chinese)

Liu S S, Liu S D (2011). Atmospheric Dynamics. 2nd ed. Beijing: Peking University Press, 92–93

Meng Z Y, Xu X D, Chen L S (1998). Mechansism of the impact of the cyclone system induced by the Taiwan Island topography on tropical cyclone unusual motion. Chin J Atmos Sci, 22(2): 156–168 (in Chinese)

Montgomery M T, Kallenbach R J (1997). A theory for vortex Rossby-waves and its application to spiral bands and intensity changes in hurricanes. Q J R Meteorol Soc, 123(538): 435–465

Montgomery M T, Nicholls M E, Cram T A, Saunders A B (2006). A vortical hot tower route to tropical cyclogenesis. J Atmos Sci, 63(1): 355–386

Montgomery M T, Smith R K (2014). Paradigms for tropical cyclone intensification. In: naval postgraduate school monterey ca dept of meteorology

Nguyen M C, Reeder M J, Davidson N E, Smith R K, Montgomery M T (2011). Inner-core vacillation cycles during the intensification of Hurricane Katrina. Q J R Meteorol Soc, 137(657): 829–844

Reasor P D, Montgomery M T, Marks F D Jr, Gamache J F (2000). Low-wavenumber structure and evolution of the hurricane inner core observed by airborne dual-Doppler radar. Mon Weather Rev, 128(6): 1653–1680

Rozoff C M, Kossin J P, Schubert W H, Mulero P J (2009). Internal control of hurricane intensity variability: the dual nature of potential vorticity mixing. J Atmos Sci, 66(1): 133–147

Schubert W H, Montgomery M T, Taft R K, Guinn T A, Fulton S R, Kossin J P, Edwards J P (1999). Polygonal eyewalls, asymmetric eye contraction, and potential vorticity mixing in hurricanes. J Atmos Sci, 56(9): 1197–1223

Shapiro L J, Willoughby H E (1982). The response of balanced

hurricanes to local sources of heat and momentum. J Atmos Sci, 39(2): 378–394

Su H, Qian C, Gu H, Wang Q (2016). The impact of tropical cyclones on China in 2015. Trop Cyclone Res Rev, 5(1–2): 1–11

Wang Y, Holland G J (1996). The beta drift of baroclinic vortices. Part II: Diabatic vortices. J Atmos Sci, 53(24): 3737–3756

Wang Y (2002). Vortex Rossby waves in a numerically simulated tropical cyclone. Part I: Overall structure, potential vorticity, and kinetic energy budgets. J Atmos Sci, 59(7): 1213–1238

Wang Y, Wu C C (2004). Current understanding of tropical cyclone structure and intensity changes—a review. Meteorol Atmos Phys, 87(4): 257–278

Wei C S, Zhao K, Yu H, Wang M J (2011). Mesoscale structure of landfall Typhoon Khanun (0515) by single doppler Radar. Chin J Atmos Sci, 35(1): 68–80 (in Chinese)

Williams G J Jr (2017). The generation and maintenance of hollow PV towers in a forced primitive equation model. In: Multidisciplinary Digital Publishing Institute Proceedings. 2017, 1(5): 156

Wu C C, Cheng H J, Wang Y, Chou K H (2009). A numerical investigation of the eyewall evolution in a landfalling typhoon. Mon Weather Rev, 137(1): 21–40

Yu J H, Tan Z M (2007). Island-like topographic effects on the propagation of vortex rossby waves. Journal of Nanjing University, 43(06):597–605 (in Chinese)

Zhang D L, Liu Y, Yau M K (1999). Surface winds at landfall of Hurricane Andrew (1992)—A reply. Mon Weather Rev, 127(7): 1711–1721

Zhang S F, Yu H, Xiang C Y (2015). Error analysis on official Typhoon intensity forecasts of CMO from 2001 to 2012. Meteorol Monogr, 41(10): 1278–1285 (in Chinese)